Fabrication and multiscale characterization of 3D silver containing bioactive glass-ceramic scaffolds

Adam C. Marsh[a], Nathan P. Mellott[a], Natalia Pajares-Chamorro[a], Martin Crimp[a], Anthony Wren[b], Neal D. Hammer[c], Xanthippi Chatzistavrou[a,*]

[a] Department of Chemical Engineering & Materials Science, Michigan State University, East Lansing, MI, USA
[b] Alfred University, Kazuo Inamori School of Engineering, Alfred, NY, USA
[c] Department of Microbiology & Molecular Genetics, Michigan State University, East Lansing, MI, USA

ARTICLE INFO

ABSTRACT

In this work, we fabricated and characterized bioactive 3D glass-ceramic scaffolds with inherent antibacterial properties. The sol-gel (solution-gelation) technique and the sacrificial template method were applied for the fabrication of 3D highly porous scaffolds in the $58.6SiO_2 - 24.9CaO - 7.2P_2O_5 - 4.2Al_2O_3 - 1.5Na_2O - 1.5K_2O - 2.1Ag_2O$ system (Ag-BG). This system is known for its advanced bioactive and antibacterial properties. The fabrication of 3D scaffolds has potential applications that impact tissue engineering. The study of the developed scaffolds from macro-characteristics to nano-, revealed a strong correlation between the macroscale properties such as antibacterial action, bioactivity with the microstructural characteristics such as elemental analysis, crystallinity. Elemental homogeneity, morphological, and microstructural characteristics of the scaffolds were studied by scanning electron microscopy associated with energy dispersive spectroscopy (SEM-EDS), transmittance electron microscopy (TEM), X-ray diffraction (XRD), X-ray photoelectron spectroscopy (XPS), Fourier transform infrared spectroscopy (FTIR), and UV-visible spectroscopy methods. The compressive strength of the 3D scaffolds was measured within the range of values for glass-ceramic scaffolds with similar compositions, porosity, and pore size. The capability of the scaffolds to form an apatite-like phase was tested by immersing the scaffolds in simulated body fluid (SBF) and the antibacterial response against methicillin-resistant *Staphylococcus aureus* (MRSA) was studied. The formation of an apatite phase was observed after two weeks of immersion in SBF and the anti-MRSA effect occurs after both direct and indirect exposure.

1. Introduction

There is a critical need to develop functional biomaterials that stimulate tissue regeneration under a variety of *in vivo* conditions. Such materials are referred to collectively as "bioactive" materials. The effectiveness of orthopedic devices increases significantly if they are bioactive and capable of developing a natural bone with the surrounding tissue. Many current orthopedic devices are based on metal and metal alloys, given they are readily available, mechanically robust, and biocompatible. However, these metal alloys cannot develop a natural bond with the surrounding tissue and can be prone to wear and corrosion that activates the foreign body reaction mechanism leading to failure [1,2]. Furthermore, metal and metal alloys are seldom used for treatments requiring complete or partial resorption [3]. For such applications, a 3D scaffold with controllable nano-to macro-scale

structure, with degradation rates matching tissue regeneration and controlled release rates of therapeutic/antibacterial agents (eg, Ag, Cu, Ga), would be considered ideal [4–6].

In particular, Ag incorporation into biomaterials has been the subject of many studies due to its broad range of antibacterial properties and the lack of bacterial resistance [7,8]. Therapeutic silver concentration [Ag] ranges from 0.1 to 1.6 ppm [9] killing off bacteria without harming eukaryotic cells. The challenge with silver is that Ag^+ ions are the most potent form, which Ag^+ ions are notoriously difficult to stabilize. However, successful stabilization of Ag^+ was achieved through the use of negatively charged aluminum tetrahedra [10]. The Ag^+ stabilization within the glass-ceramic structure further showed that Ag^+ ions were released in a controlled manner, thus making it a suitable approach for Ag^+ ions incorporation.

In addition, a 3D open porous scaffold with interconnected porosity

can provide the required pathway to the surrounding tissue to migrate and reconstruct the lost or defected tissue throughout the whole volume. It is anticipated the chemical, morphological, and microstructural properties of the scaffold need to offer the necessary signals for cell proliferation and differentiation that can lead to the regeneration of functional tissue. Given their potential to satisfy bioactivity and biodegradability, glasses and glass ceramics, particularly those within and based upon the $60SiO_2$ - $4P_2O_5$ - $36CaO$ (wt%) compositional system, have garnered attention within the biomaterial community as potential candidate materials for 3D scaffolds fabrication [11,12]. It has been shown that the degradation rate of such glasses and glass-ceramic scaffolds can be controlled by tailoring the composition and atomic-scale structure of the materials [13]. In addition, the nano-to macro-scale 3D structure of the scaffold is typically controlled through scaffold processing and has a direct effect on scaffold properties [14].

There are numerous techniques to fabricate 3D scaffolds. Sol-gel based methods are ideal for glass and glass-ceramic scaffold processing, given they afford the realization of scaffolds with (1) a wide range of compositions, (2) controllable nano-to macro-structure, (3) an easy to scale up the approach, and (4) the ability to include therapeutic or antibacterial agents, such as heavy metal ions and antibiotics. Solution-based fabrication has been used to fabricate mesoporous 3D scaffolds with surface areas $> 100 \, m^2/g$ [15,16], as the rate of bioactivity increases when the surface area to volume ratio increases [17–19]. The sol-gel technique often takes advantage of sacrificial templates for the fabrication of 3D glass or glass-ceramic scaffolds [15,17,18,20–22]. Polyurethane foams are often used as templates because they can be manipulated to produce a scaffold with optimal three-dimensional networks. The aforementioned characteristics develop the ability to control the multiscale structure of scaffolds, which is paramount as structure-property relationships must be clearly understood. For example, it has been shown that scaffold connectivity, scaffold strut integrity, scaffold matrix structure, and the structural role of any therapeutic/antibacterial agent all affect the bioactivity and therapeutic ion release [23].

In this paper 3D bioactive glass-ceramic scaffolds containing silver ions for potential biological and antibacterial applications are fabricated and characterized. These scaffolds are prepared using a sol-gel based sacrificial template method. The structure of these scaffolds was characterized over multiple length scales (500 microns to ∼50 nanometers) using a variety of complementary microscopic and spectroscopic techniques. The bioactivity of the scaffolds was confirmed through *in vitro* exposure to simulated body fluid followed by morphological and chemical examination. This work also examines the micro- and macro-structural characteristics of a novel sol-gel derived Ag-BG 3D scaffold and the resulting bioactive and anti-MRSA properties.

2. Materials and methods

2.1. Fabrication

The scaffold composition is based on a silver-containing bioactive glass-ceramic (Ag-BG) in the $58.6SiO_2$ - $24.9CaO$ - $7.2P_2O_5$ - $4.2Al_2O_3$ – $1.5Na_2O$ − $1.5K_2O$ – $2.1Ag_2O$ (wt%) system (Table 1) that has been previously studied [9]. The glass-ceramic scaffolds were prepared using the sacrificial template method and applying a specific heat treatment to the solution coated polymeric foams, as outlined by Zhu et al. [16]. The preparation of the sol-gel glass-ceramic in the solution stage has been previously described [24]. Briefly, the sol-gel bioactive glass 58S at the solution stage (in the system $58SiO_2$ – $33CaO$ – $9P_2O_5$ (wt.%)) is mixed with the solution stage of a sol-gel derived glass-ceramic in the system $60SiO_2$ – $6CaO$ – $3P_2O_5$ - $14Al_2O_3$ – $7Na_2O$ – $10K_2O$ (wt.%), where the fabrication of each solution has been previously described [24,25]. After mixing the two sol-gel precursors, the resulting solution was stirred for 17 h to ensure homogeneity. The 3D glass-ceramic

Table 1
The nominal composition of Ag-BG glass-ceramic scaffolds.

	Weight % Oxide	Mol% Oxide		Atom%
SiO_2	58.6	61.5	Si	20.9
P_2O_5	7.2	4.3	P	2.9
Al_2O_3	4.2	2.6	Al	1.8
CaO	24.9	28.0	Ca	9.5
Na_2O	1.5	1.5	Na	1.0
K_2O	1.5	1.0	K	0.7
AgO	2.1	1.1	Ag	0.7
			O	62.4

scaffolds were prepared by the sacrificial template technique [16] through the calcination of Ag-BG solution coated polyurethane foams. In brief, polyurethane foam (45 pores per inch; United Plastics) was cut into $25.4 \times 25.4 \times 25.4$ mm cubes, immersed in ethanol and ultrasonically cleaned for 15 min. The foams were dried at 60°C for 15 min and soaked in the previously described combined sol-gel solution for approximately 2 min. The foams were then removed from the solution, compressed by 50% in each principal axis for 5 s to release excess sol-gel solution and placed in an oven at 60 °C for 2 min. This process was repeated in each sample six times. The coated foams were allowed to dry at 60°C for 24 h to ensure the solution was properly gelled. The applied heat treatment (Fig. 1) subjected the coated foams to a temperature of 400°C with heating rate $2 \, °C \, min^{-1}$ and holding time of 1 h to burn out the polyurethane foam before preceding to 700°C with the same heating rate and holding time of 5 h. The drying and heat treatment applied to the resultant, coated foams, is shown in Fig. 1. These scaffolds will be referred in the text as "Ag-BG scaffolds", where Ag-BG refers to silver-containing bioactive glass. The heat treatment allowed for the sacrificial template to be removed, leaving behind a 3D glass-ceramic structure with open and interconnected porosity.

2.2. Characterization

Scaffolds were characterized using a variety of microscopic and spectroscopic techniques. Optical microscopy (OM; VHX-600 E Digital Microscope) and scanning electron microscopy (SEM; Zeiss LS25 EVO/Auriga XB and JEOL JSM-IT500) were utilized to image the scaffolds on the millimeter to nanometer scale respectively. SEM images were collected at accelerating voltages less than or equal to 20 kV. In addition, energy dispersive spectroscopy (EDS; Ametek EDAX Apollo X) was utilized to semi-quantitively assess the micro-scale chemical homogeneity of the scaffolds. All EDS maps were collected at less than or equal to 20 keV with a step size of 126.2 eV. TEM analysis was performed using a JEOL 100CX microscope using pulverized samples on 200 mesh copper grids with carbon support film (Electron Microscopy Sciences, CF200-CU) under a voltage of 120 kV. Compressive strength was measured using a Rheometric Solids Analyzer (RSA-III) instrument with a load of 2 kg with a crosshead speed of $0.5 \, mm \, min^{-1}$.

X-ray diffraction (XRD; Rigaku Smartlab) was performed on powdered samples to examine the structure and crystallinity of the scaffolds. Diffraction patterns were collected from 10° to 90° 2θ using Cu $K\alpha$ radiation at 40 kV and 44 mA. Furthermore, the molecular structure of the powdered scaffolds was examined using Fourier transform infrared – attenuated total reflection where samples were placed on top of a diamond crystal and 10,000 psi was applied to ensure the powder had adequate contact with the crystal before performing the measurement (FTIR-ATR; Jasco FT/IR-4600). Absorbance IR spectra were collected from 4000 to $400 \, cm^{-1}$ with a resolution $2 \, cm^{-1}$. X-ray photoelectron spectroscopy (XPS; PerkinElmer Phi 5400), using non-monochromatic Al K_α radiation X-rays was performed to investigate the chemical structure of the silver within the scaffold. High-resolution Ag_{3d} spectra were collected with a pass energy of 29.35 eV and a step size of 0.125 eV, with peak position normalized to a C_{1s} signal of 284.6 eV.
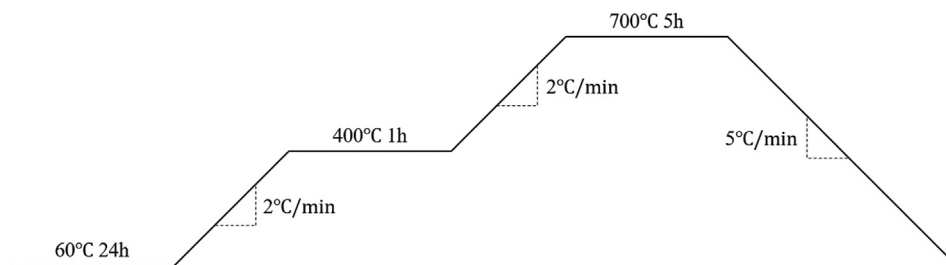
Fig. 1. Heat treatment applied for the fabrication of Ag-BG scaffolds.
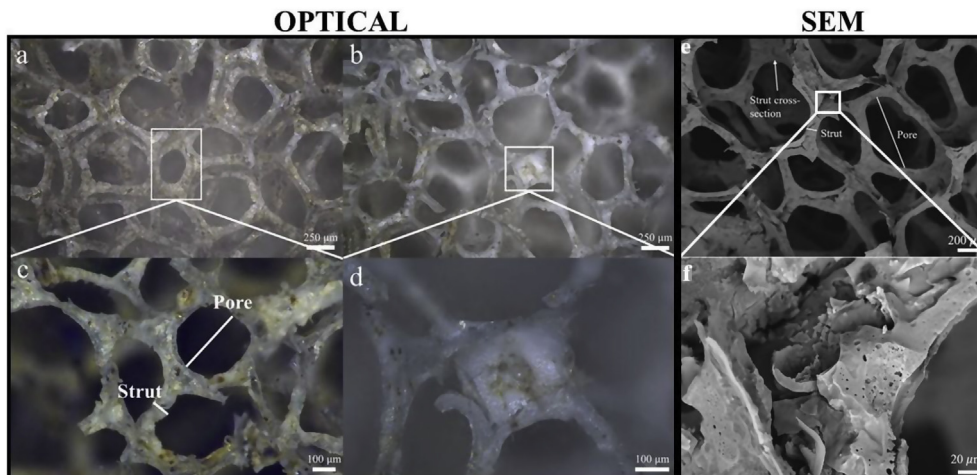

Fig. 2. Optical images of the fracture surface of an Ag-BG scaffold at (a,b) 100x, (c) 300x, and (d) 500x. Back-scattered SEM images of the fracture surface of an Ag-BG scaffold at low (e) and high magnification (f).

Ultraviolet and visible spectroscopy (UV-VIS; Lambda900) was used to further examine the chemical structure of silver. Absorption spectra were collected from 350 to 600 nm.

The porosity of the 3D scaffolds was calculated using the following equation:

$$V_{AIR}/V_{TOTAL} * 100 = \% \text{ Porosity} \tag{1}$$

where V_{TOTAL} was the dimensions of the scaffold in the three principal directions, V_{AIR} was the empty volume found by subtracting V_{TOTAL} from V_{GLASS}, and V_{GLASS} was found by dividing the mass of the scaffold by the density of the glass. The density of Ag-BG glass was measured by N_2 pycnometry (AccuPyc II 1340). Ag-BG powder was placed inside the chamber before it was purged 5 times using N_2 gas. N_2 was added to the chamber at a rate of 0.1 psig min^{-1} to determine the density and repeated 20 times to obtain an average density of the glass.

The capability of the scaffolds to form an apatite-like phase on their surface was studied by immersing the scaffolds in simulated body fluid (SBF) at a pH of 7.26 at 37.5 °C, which is a well-established protocol in biomaterials science. SBF was utilized to mimic human plasma with the following ionic concentrations: $142.0Na^+$, $5.0 K^+$, $2.5Ca^{2+}$, $1.5Mg^{2+}$, $148.8Cl^-$, $1.0HPO_4^-$, $4.2HCO_3^-$, and $0.5 SO_4^{2-}$ (mmol dm^3) and prepared as previously described by Kokubo et al. [26,27]. The scaffolds were exposed to SBF using a mass to volume ratio of 1:1 at 174 RPM and 37.5 °C for 14 days; with SBF replacement every 48 h. SEM and EDS were then used to examine the resulting scaffolds for evidence of CaP formation.

The anti-MRSA effect of the scaffold was studied directly by inoculating bacteria in the nutrient broth and leaving at 37°C overnight to allow growth. The optical density of the MRSA was measured and adjusted to be 10^8 cells mL^{-1} in PBS. The MRSA in PBS was exposed to 11.0 mg of the Ag-BG scaffold and incubated for 24 h at 37°C. The supernatant was collected, and serial ten-fold dilutions performed in a 96-well plate. All serial-dilutions were platted on nutrient agar plates and incubated at 37°C for 24 h. Bacterial growth was assessed by colony forming units (CFU).

The anti-MRSA effect of the scaffold was also indirectly evaluated by placing 50 mg of the Ag-BG scaffold into 8 mL of PBS and leaving at 37°C for up to 21 days, with 50% of the solution collected every three days while the solution was renewed with an equal volume of fresh PBS. The collected volumes were characterized as extracts and are expected to have incorporated ions that were released from the scaffolds. MRSA in 1 mL of PBS was exposed to an equal volume of the extracts collected at specific times. A culture of MRSA was prepared as previously described which after 24 h of incubation at 37°C, was serial ten-fold diluted in a 96-well plate and plated on nutrient agar plates. The plates were then incubated at 37°C for 24 h and bacteria growth was assessed by counting the CFU.

The concentration of [Ag^+] ions in the extracts was also measured by Inductively Coupled Plasma Optical Emission Spectrometer [(ICP-OES) - Perkin Elmer]. All antibacterial tests were performed in biological and technical triplicates.

3. Results

The surface morphology of the Ag-BG scaffold fracture surfaces was examined from the millimeter to ~50 nm scale using both optical and electron microscopy.

The optical microscopy images (Fig. 2a–d) show that the scaffolds exhibit connectivity, with microscale cracks and open pores. The struts and intersections of the scaffolds exhibit heterogeneous color intensities, with dark coloration in the centre of the struts and light coloration on the outside of the struts. The struts and intersections of the scaffolds dark colored, < 10 µm–1 µm size circular/oblong features, some of which exhibit a yellow/brown sheen (Fig. 2d). The scaffolds themselves exhibit a microscale distribution of transparent and translucent sheen (Fig. 2a–d). The average strut width is 85 ± 16 µm and
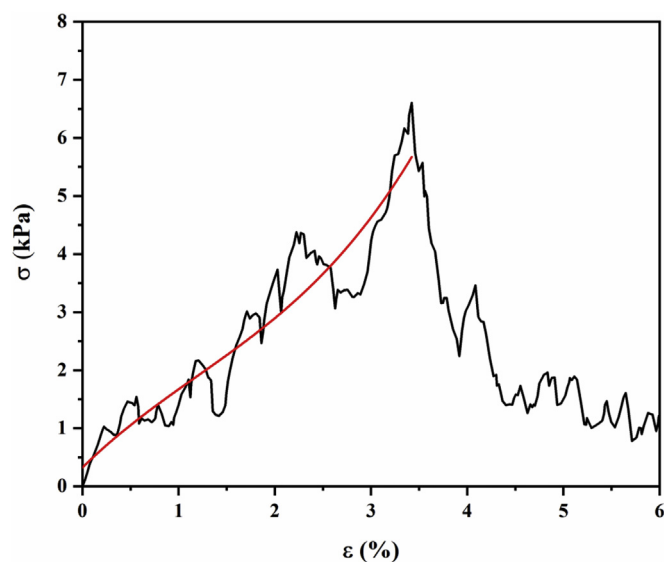
Fig. 3. Stress-strain curve of an Ag-BG scaffold representative of the compressive strength of the Ag-BG scaffolds (red line is a guide to the eye).

the average pore diameter is 504 ± 126 μm (n = 20), as measured from SEM back-scattered images (Fig. 2e). The overall scaffold porosity was calculated to be 98% using the value 2.78 g cm^{-3} for Ag-BG density and equation (1). The lack of any areas of high atomic number (Z) in the images both in low and high magnification (Fig. 2e and f, respectively) also indicates microscale elemental homogeneity in the Ag-BG scaffolds. Fig. 2f shows cracking on the interior of the struts as well as around the exterior of the overall structure, where porosity is observed with pores < 10 μm in diameter. The compressive strengths of the Ag-BG scaffolds were measured from the stress-strain curves at 4.4 kPa (Fig. 3).

A secondary electron SEM image and corresponding EDS X-ray maps of a representative Ag-BG fracture surface are shown in Fig. 4. The elemental maps suggest homogeneous distribution of Si, Ca, P, Al, and Ag on the micron scale. Nevertheless, high-resolution SEM back-scattered electron images of the fracture surface of an Ag-BG scaffold shown in Fig. 5a and b feature varying contrast at a scale of < 200 nm, suggesting some heterogeneity at the fine scale. EDS X-Ray maps indicate that these lighter areas are aggregates of Ag (Fig. 5c). Further analysis at the nanoscale using TEM presents a clearer perspective of the scaffold's structure (Fig. 6a). Diffraction ring analysis shows that both metallic silver and hydroxyapatite are the present (Fig. 6b).

To further analyze the crystalline phases in the Ag-BG scaffolds, the XRD pattern is shown in Fig. 7. All peak positions correspond to crystals

within The International Centre for Diffraction Data (ICCD) and indicates that the crystalline components of the scaffolds are a combination of a hydroxyapatite phase (peaks marked with black squares, 26.7, 28.1, 32.3, and 46.8 2θ; PDF No. 9003552), cristobalite (peaks marked with black circles), and metallic silver (peaks marked with black triangles, 37.9, 44.1, 64.3, and 77.1 2θ; PDF No. 01-071-4613). It should be noted that peaks with a lower signal to noise ratio were not matched against the ICCD database. It is worth noting that the background intensity increases with decreasing 2θ. FTIR-ATR spectra of powdered Ag-BG is shown in Fig. 8. The deconvoluted spectrum displays broad peaks centered at ~1030, ~800, and ~450 cm^{-1}, with clear shoulders centered at approximately 1210 and 940 cm^{-1}. Dashed lines are shown in Fig. 8 to guide the eye for qualitative peak deconvolution. The characteristic vibration modes of a silicate network are the only features in the IR spectrum of the Ag-BG scaffold [28].

An XPS survey spectrum of the surface of an Ag-BG fracture surface was collected (not shown) revealing all of the expected, major elements. In addition, a high-resolution scan within the Ag$_{3d}$ region (377-357 eV) was collected and is shown in Fig. 9a. Clear peaks are observed at 367.7 and 373.5 eV, corresponding to Ag$_{3d\ 5/2}$ and Ag$_{3d\ 3/2}$ [29]. Fig. 9b shows UV-VIS spectra collected from powdered Ag-BG scaffolds, showing a clear absorbance peak at 428 nm that is correlated with the presence of metallic Ag in the structure [30].

Secondary electron images of Ag-BG fracture surfaces, before and after soaking in SBF for 14 days, are shown in Fig. 10. The fracture surface of the scaffold prior to reaction exhibits a relatively featureless surface, with the exception of pores of less than 10 μm in diameter (Fig. 10a). The representative image of a post-reaction fracture surface exhibits a morphology of ~150–500 nm spherical to cylindrical features that are cauliflower-like (Fig. 10b). EDS spectra (not shown) show that these features are composed primarily of Ca and P with Ca/P ratio slightly higher than 1.67, which is the ratio for the stochiometric hydroxyapatite. The formation rate of this apatite-like layer is under current investigation, while the thickness of this layer is expected to be lower than the EDS interaction volume (< 5 μm) as the EDS spectrum identifies also ions from the Ag-BG scaffolds. The Ca-P deposition after the immersion in SBF is also confirmed by the FTIR spectra in Fig. 10c, where the dual-peak at 569-609 cm^{-1} is assigned to an apatite-like phase (green line) [28]. As it was expected the characteristics bands of the Si–O bending and Si–O–Si stretching are still observed in the FTIR spectrum after immersion in SBF, because scaffolds were pulverized, and the powder was used for the measurements. Thus, not only the Ca–P deposited phase was identified but the silicate structure as well. This dual peak is not present in the FTIR spectrum of the scaffolds before immersion in SBF (red line). The comparison of Ag-BG scaffolds bioactivity to the respect of other BG scaffolds was not the aim of the current work.
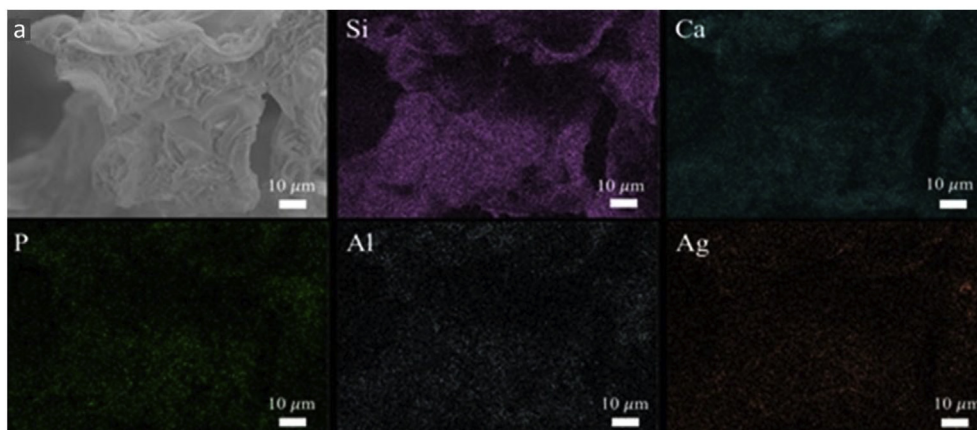

Fig. 4. Representative secondary electron image and corresponding EDS x-ray maps of the fracture surface of an Ag-BG scaffold.
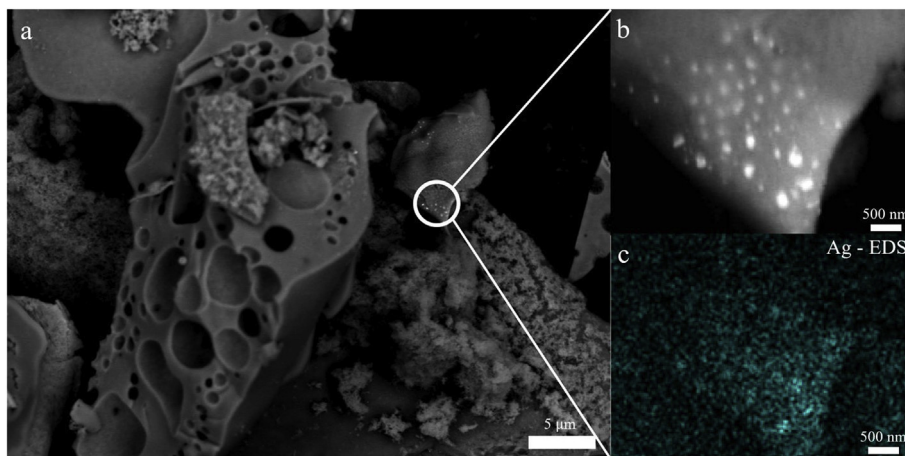
Fig. 5. High-resolution back-scattered electron images of the fracture surface of an Ag-BG scaffold at (a) 3700x low and (b) 30,000x high magnification. (c) Corresponding EDS x-ray maps of Ag of the Ag-BG scaffold fracture surface.

The antibacterial properties of the Ag-BG scaffolds against MRSA are presented in Fig. 11. The direct test, where the MRSA was exposed to Ag-BG scaffolds, showed a significant decrease in bacteria viability after 24 h of exposure (Fig. 11a). The indirect test, where the MRSA was exposed to the extracts of the scaffold from different time points, showed inhibition that decreased with increasing extract time (Fig. 11b). Likewise, the concentration of Ag in the extracts [Ag] was observed to decrease with increasing time (Fig. 11b, red symbols). In particular, the concentration of [Ag] was measured at 0.45 ppm on the 3rd day and it was held on cytotoxic for the bacteria concentration (0.18 ppm) for up to the 12th day. When immersions are higher than 15 days there is a decrease in the concentration of silver [Ag] to values lower than 0.1 ppm, which is the minimum required to show significant bactericidal activity. All these values were constantly lower than the upper threshold (1.6 ppm) for cytotoxic behavior to eukaryotic cells. The red dash line in Fig. 11b serves as a guide to the eye showing the decrease in Ag ion concentration with the immersion time.

4. Discussion

This study presents the fabrication and characterization of 3D scaffolds in a unique composition that incorporates Ag ions within a silicate glass-ceramic structure. The sacrificial template technique was applied, and the structural, chemical, mechanical, bioactive, and antibacterial characteristics were assessed. Structural analysis of the scaffold at scales greater than approximately 100 microns focused primarily on scaffold strut size and geometry, as well as pore size and shape
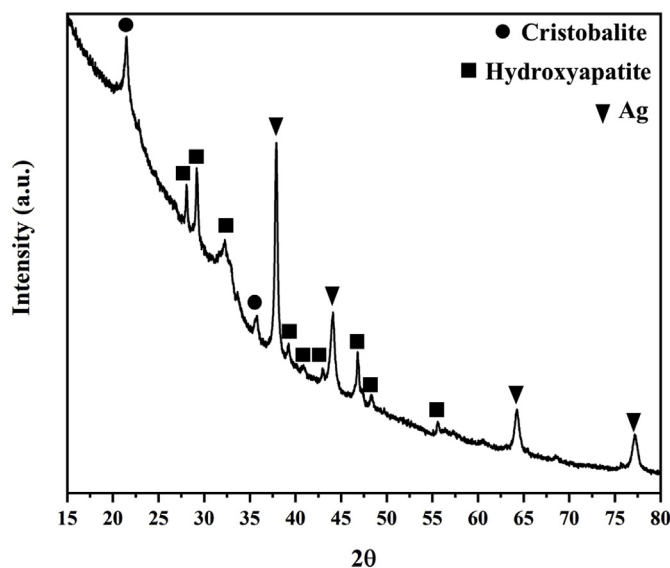

Fig. 7. XRD pattern of powdered Ag-BG scaffolds.

(Fig. 2). Using these measurements, the porosity of these scaffolds was determined to be higher than 90%. These highly porous scaffolds are expected to enhance cell migration and spreading when used in _in vivo_ applications [31]. However, the compressive strength of the Ag-BG
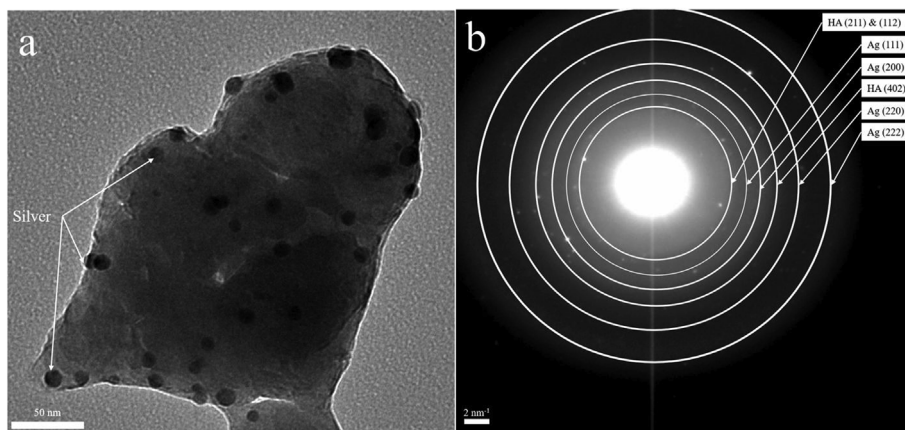

Fig. 6. TEM bright field image (a) of the Ag-BG scaffold and the diffraction pattern (b) show the microstructure at the nanoscale (a).
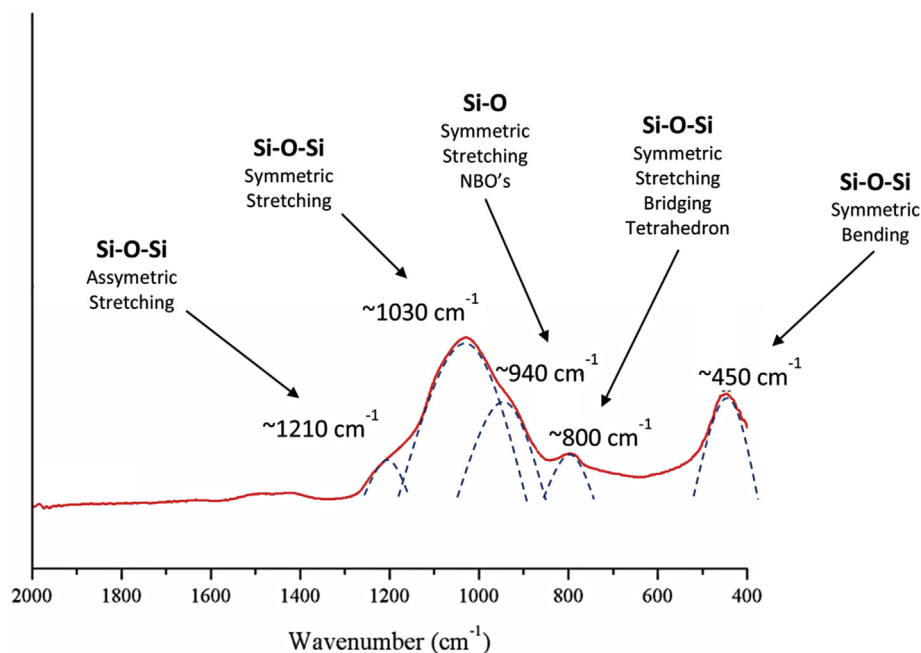
Fig. 8. FTIR absorbance spectra of powdered Ag-BG scaffolds; dashed lines are shown to guide the eye for qualitative peak deconvolution.
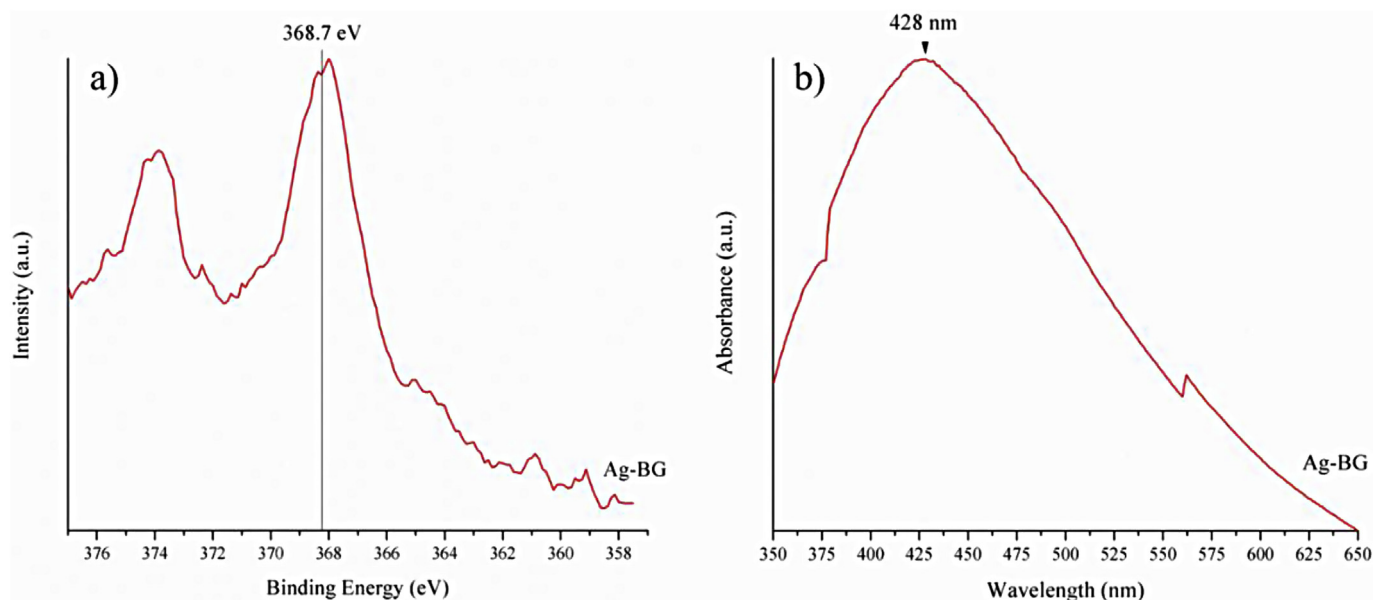

Fig. 9. High-resolution XPS (Ag_{3d}) spectra of powdered Ag-BG scaffolds (a) and UV-VIS absorbance (b).

scaffolds (Fig. 3) was measured to be at the lower end of the range for such highly porous scaffolds with similar compositions [32,33], indicating the requirement to use these new scaffolds in small defects or low-load bearing applications.

Optical microscopy (Fig. 2) revealed spatial inhomogeneity of the fracture surface sheen and overall translucency, which may be evidence of the presence of both amorphous and crystalline components. In addition, under optical microscopy, the color intensity varies spatially with the "inside" of the struts appearing darker than the outside (Fig. 2a and b). This could be the result of surface oxidation and reduction of silver, inhomogeneous distribution of crystalline phases, and/or cracking and pores present on the fracture surface. However, EDS maps (Fig. 4) suggest homogeneous distribution of all elements on the scale higher than 10 μm, suggesting that the variety in color intensity to primarily be the result of surface morphological characteristics.

Furthermore, imaging using backscattered electrons (Fig. 2e and f) at comparable magnifications to the optical microscope images further support this hypothesis.

Fracture surfaces of the scaffold struts clearly exhibit circular to oblong dark areas less than 25 microns in size. Upon further investigation using high-resolution BSE imaging (Fig. 5), these areas are shown to be micron to submicron pits in the surface. The circular to oblong pits appear to contain either open space or are partially or completely filled with particulate material. High magnification images (Fig. 5a) of regions with both empty and filled pores suggest that the particulates within the "filled" pores are a material which has a much higher atomic number Z than the surrounding matrix (Fig. 5b). Given the system used here, the bright areas shown in Fig. 5b are silver, or silver dominated, nanoparticles, which is consistent with the TEM images (Fig. 6). The silver ion localization is most likely a result of the
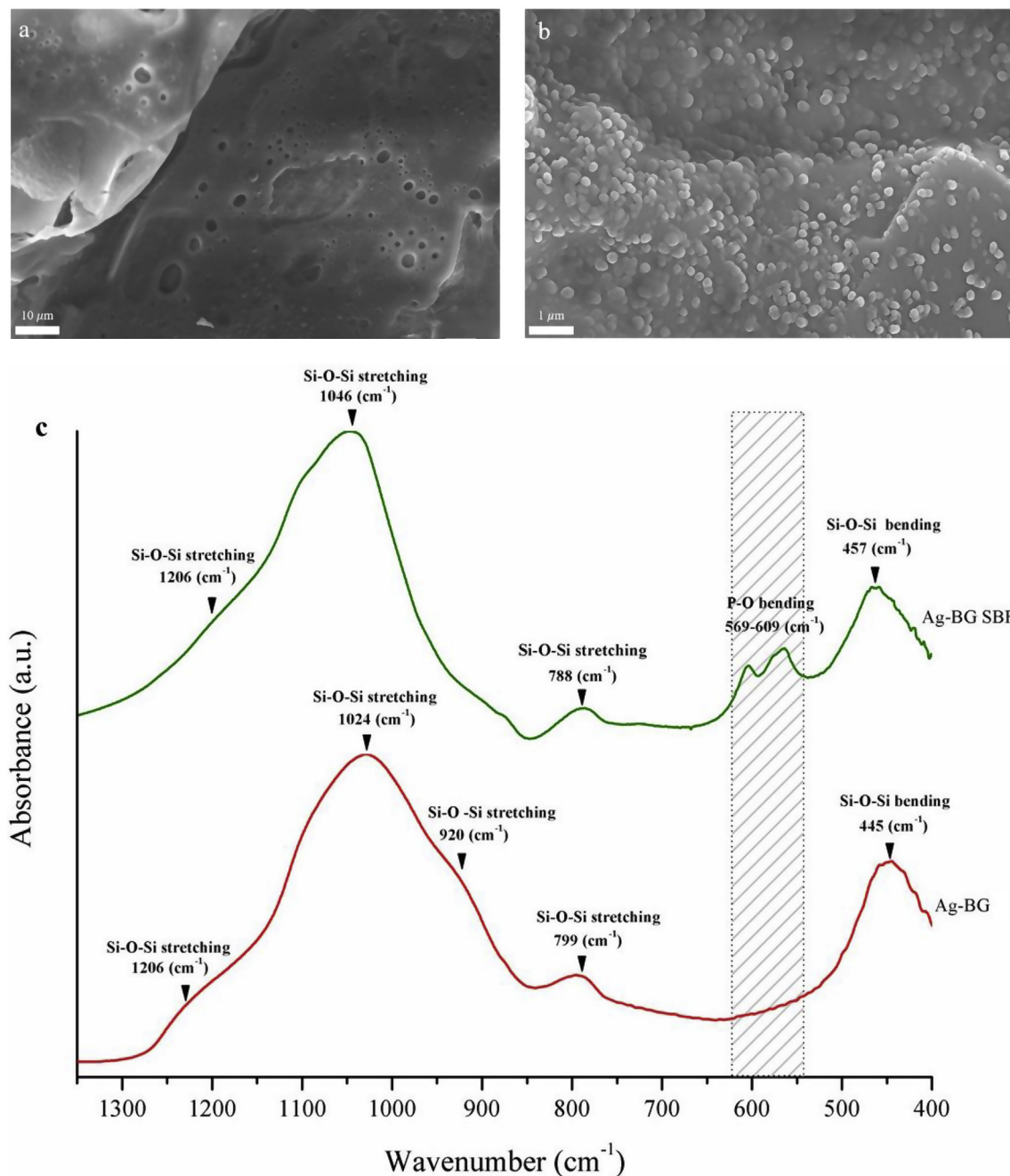
Fig. 10. Secondary electron images of the fracture surface of Ag-BG scaffold (a) prior to and (b) post SBF immersion for 14 days. (c) FTIR spectra before (red line) and after (green line) the immersion in SBF.

presence of negatively charged aluminum tetrahedra stabilizing Ag ions, thus making Ag agglomeration difficult. This has been previously studied by Chatzistavrou et al. [9] where Aluminum NMR (nuclear magnetic resonance) showed that the presence of Ag caused an increase in the five-fold coordination of the Al, which was correlated to Ag-stabilized aluminum tetrahedrons. Moreover, our work highlights the importance of the specific order the reagents were added during the fabrication process as well as the stirring time. However, the applied heat treatment during the scaffold fabrication process provided conditions to overcome the stabilizing forces localizing silver ions that allowed silver to be reduced to metallic Ag nanoparticles [10,34]. The TEM diffraction pattern (Fig. 6b) also indicates the presence of hydroxyapatite as an additional crystalline phase. XRD and FTIR were used in combination to further investigate the overall scaffold structure on the

atomic to the molecular scale. It is clear from diffraction results the scaffold is composed of crystalline phases. Interestingly, cristobalite is also observed in the XRD diffraction patterns; the formation of this phase is attributed to the presence of silver and its action as catalyst inducing cristobalite formation at relatively low temperatures [35]. Additionally, FTIR was used to further confirm the presence of the amorphous component and investigate its molecular structure [36]. It is clear from the FTIR data (Fig. 8) that the silicate glass consists of interconnected silicate tetrahedra with both bridging and non-bridging oxygen species. This is consistent with what has been previously reported for sol-gel glass-ceramic powders within similar systems [24,37,38].

Matching of the experimental diffraction patterns to standard PDF cards suggests that in addition to silicate glass, the scaffold matrix
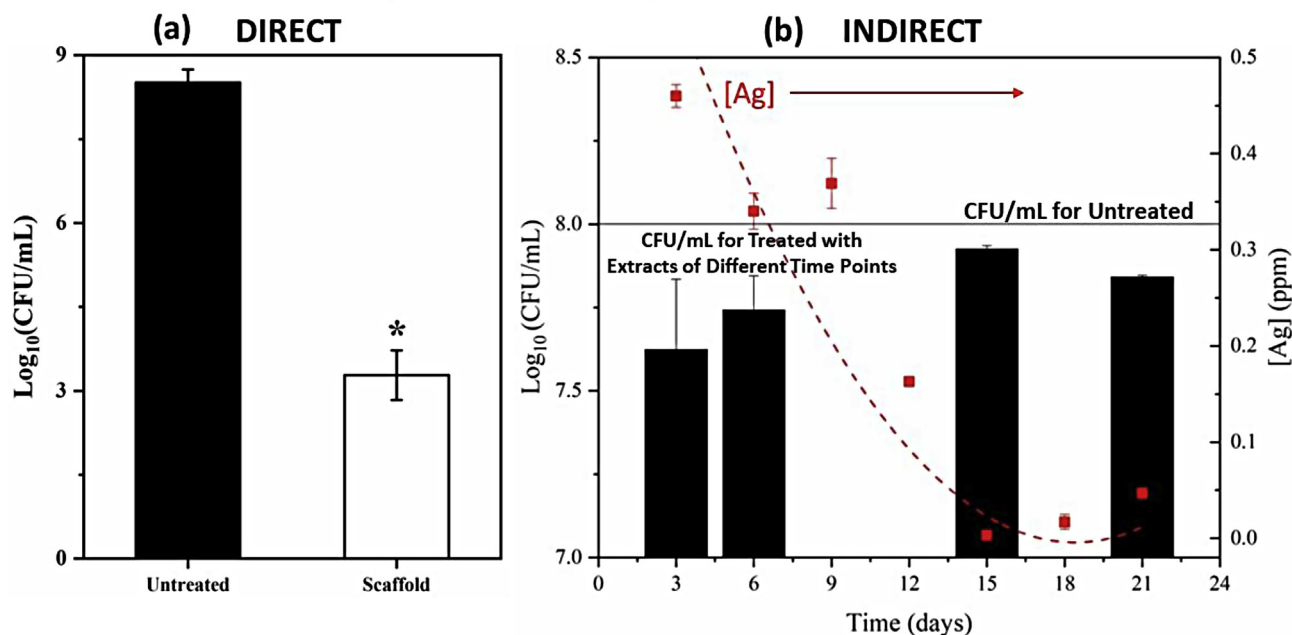
Antibacterial Tests

Fig. 11. Anti-MRSA characteristics of the Ag-BG scaffolds under direct (a) and indirect (b) tests. The red symbols in (b) show the Ag concentration in the extracts of the Ag-BG scaffolds that is decreased with the time (red slashed line is the guide to the eye).

contains crystalline hydroxyapatite, cristobalite, and metallic silver. However, it is worth noting that the peak at 26.7 2θ (Fig. 7) has been assigned to Ag_2O_4 when observed in spectra of similar systems [9]. Therefore, in addition to the other phases, it is also conceivable that silver oxide may also be present. Hydroxyapatite formation, while minimal as evidenced from TEM images (Fig. 6b) and the broad rings in diffraction patterns, can result from the applied heat treatment and the relevant concentrations of the Ca, P ions in the structure [39,40]. Similarly, the formation of metallic silver indicates that the stabilization of silver ions cannot be preserved under the given processing conditions.

Additional characterization of the metallic silver was performed given its inclusion was to induce therapeutic/antibacterial properties. It has been suggested the overall size, shape, and chemistry of the silver ions and/or particles have a significant effect on the therapeutic/antibacterial performance of Ag-containing biomaterials. Both the XPS and the UV-VIS results suggest silver is primarily in the form of metallic nanoparticles, however, possible contributions from silver oxide and/or ionic silver within the glass structure cannot be ruled out, as a homogeneous distribution of Ag within the scaffolds is observed with the EDS mapping analysis (Fig. 4).

The deposition of an apatite-like phase on the surface of the Ag-BG scaffolds, after 14 days of immersion in SBF, was confirmed by SEM and FTIR analysis (Fig. 10). SEM images revealed increased roughness associated with the formation of cauliflower-like structures on the surface. The formation of these morphological features occurred due to deposition during SBF exposure. These deposits were determined to be an apatite-like phase, as evidenced by the dual Ca–P peak at ~570-610 cm^{-1} in the FTIR spectrum. Finally, significant antibacterial properties were observed when MRSA was directly exposed to the novel Ag-BG scaffolds (Fig. 11a). It is very important that Ag-BG scaffolds can inhibit an antibiotic-resistant strain that has been reported as the most common in orthopedic infections. The effectiveness of Ag-BG to combat oral bacteria has been well presented in our previous work [9]. However, the capability of this system to combat MRSA expands the spectrum of potential applications into orthopedics. This characteristic is primarily attributed to the Ag in the scaffold's structure. The leaching of

the ions from the scaffolds is expected to be controlled so that the pH value remains consistently neutral. The scaffold is expected to degrade over time. As previously was observed the degradation of Ag-BG pellets [9] led to a weight loss of 16% after 45 days of immersion in TRIS-buffer. The 3D scaffolds present an increase in the surface to volume ratio that can increase the degradation rate. The degradation profile of these scaffolds immersed in different aqueous solutions will be studied in future work as it seems to affect the indirect antibacterial properties. In particular, the indirect antibacterial test (Fig. 11b) correlates the antibacterial activity with the release of Ag with time. The concentration of Ag in the extracts decreased with time, which agrees with the antibacterial activity of the extracts that also decreased with time.

In summary, this work highlights the microstructural characteristics, bioactive, and antibacterial properties of novel Ag-BG scaffolds. Conditions during the processing lead to structural characteristics that significantly affect the overall bioactive and bactericidal behavior of these scaffolds.

5. Conclusions

The fabrication of 3D scaffolds using a novel bioactive and antibacterial composition (Ag-BG) has been achieved. Structural characteristics from the nano-to macro-scale affect the overall performance of these scaffolds. Processing has a significant impact on the microstructural characteristics, such as the status of Ag in the structure and the formation of the specific crystalline phases. The overall bioactive and antibacterial characteristics could potentially allow the use of these scaffolds in biological applications against MRSA and towards tissue regeneration.

Conflict of interest

Authors have no conflict of interest.

Acknowledgments

Authors would like to acknowledge Dr. Per Askeland for his

References

[1] J.M. Anderson, A. Rodriguez, D.T. Chang, Foreign body reaction to biomaterials, Semin. Immunol. 20 (2) (2008) 86–100, https://doi.org/10.1016/j.smim.2007.11.004.

[2] J.J. Jacobs, J.L. Gilbert, R.M. Urban, Corrosion of metal orthopaedic implants, J. Bone Joint Surg. Am. 80 (2) (1998) 268–282.

[3] B. Stevens, Y. Yang, A. Mohandas, B. Stucker, K.T. Nguyen, A review of materials, fabrication methods, and strategies used to enhance bone regeneration in engineered bone tissues, J. Biomed. Mater. Res. B Appl. Biomater. 85 (2) (2008) 573–582, https://doi.org/10.1002/jbm.b.30962.

[4] S. Bose, M. Roy, A. Bandyopadhyay, Recent advances in bone tissue engineering scaffolds, Trends Biotechnol. 30 (10) (2012) 546–554, https://doi.org/10.1016/j.tibtech.2012.07.005.

[5] S.J. Hollister, Porous scaffold design for tissue engineering, Nat. Mater. 4 (7) (2005) 518–524, https://doi.org/10.1038/nmat1421.

[6] J.R. Jones, L.M. Ehrenfried, L.L. Hench, Optimising bioactive glass scaffolds for bone tissue engineering, Biomaterials 27 (7) (2006) 964–973, https://doi.org/10.1016/j.biomaterials.2005.07.017.

[7] H.H. Lara, N.V. Ayala-Núñez, L.d.C. Ixtepan Turrent, C. Rodríguez Padilla, Bactericidal effect of silver nanoparticles against multidrug-resistant bacteria, World J. Microbiol. Biotechnol. 26 (4) (2010) 615–621, https://doi.org/10.1007/s11274-009-0211-3.

[8] M. Rai, A. Yadav, A. Gade, Silver nanoparticles as a new generation of antimicrobials, Biotechnol. Adv. 27 (1) (2009) 76–83 https://doi.org/10.1016/j.biotechadv.2008.09.002.

[9] X. Chatzistavrou, J.C. Fenno, D. Faulk, S. Badylak, T. Kasuga, A.R. Boccaccini, P. Papagerakis, Fabrication and characterization of bioactive and antibacterial composites for dental applications, Acta Biomater. 10 (2014) 3723–3732, https://doi.org/10.1016/j.actbio.2014.04.030.

[10] M. Kawashita, S. Tsuneyama, F. Miyaji, T. Kokubo, H. Kozuka, K. Yamamoto, Antibacterial silver-containing silica glass prepared by sol-gel method, Biomaterials 21 (4) (2000) 393–398, https://doi.org/10.1016/S0142-9612(99)00201-X.

[11] J.E. Gough, J.R. Jones, L.L. Hench, Nodule formation and mineralisation of human primary osteoblasts cultured on a porous bioactive glass scaffold, Biomaterials 25 (11) (2004) 2039–2046 https://doi.org/10.1016/j.biomaterials.2003.07.001.

[12] C. Gao, T. Liu, C. Shuai, S. Peng, Enhancement mechanisms of graphene in nano-58S bioactive glass scaffold: mechanical and biological performance, Sci. Rep. 4 (2014) 4712, https://doi.org/10.1038/srep04712.

[13] M. Hamadouche, A. Meunier, D.C. Greenspan, C. Blanchat, J.P. Zhong, G.P. La Torre, L. Sedel, Long-term in vivo bioactivity and degradability of bulk sol-gel bioactive glasses, J. Biomed. Mater. Res. 54 (4) (2001) 560–566, https://doi.org/10.1002/1097-4636(20010315)54:4<560::AID-JBM130>3.0.CO;2-J.

[14] J.R. Jones, L.L. Hench, Factors affecting the structure and properties of bioactive foam scaffolds for tissue engineering, J. Biomed. Mater. Res. B Appl. Biomater. 68 (1) (2004) 36–44, https://doi.org/10.1002/jbm.b.10071.

[15] C. Wu, Y. Zhou, W. Fan, P. Han, J. Chang, J. Yuen, M. Zhang, Y. Xiao, Hypoxia-mimicking mesoporous bioactive glass scaffolds with controllable cobalt ion release for bone tissue engineering, Biomaterials 33 (7) (2012) 2076–2085, https://doi.org/10.1016/j.biomaterials.2011.11.042.

[16] Y.F. Zhu, C.T. Wu, Y. Ramaswamy, E. Kockrick, P. Simon, S. Kaskel, H. Zrelqat, Preparation, characterization and in vitro bioactivity of mesoporous bioactive glasses (MBGs) scaffolds for bone tissue engineering, Microporous Mesoporous Mater. 112 (1–3) (2008) 494–503, https://doi.org/10.1016/j.micromeso.2007.10.029.

[17] C. Wu, R. Miron, A. Sculean, S. Kaskel, T. Doert, R. Schulze, Y. Zhang, Proliferation, differentiation and gene expression of osteoblasts in boron-containing associated with dexamethasone deliver from mesoporous bioactive glass scaffolds, Biomaterials 32 (29) (2011) 7068–7078, https://doi.org/10.1016/j.biomaterials.2011.06.009.

[18] Y. Zhu, S. Kaskel, Comparison of the in vitro bioactivity and drug release property of mesoporous bioactive glasses (MBGs) and bioactive glasses (BGs) scaffolds, Microporous Mesoporous Mater. 118 (2009) 176–182, https://doi.org/10.1016/j.micromeso.2008.08.046.

[19] X. Li, X. Wang, H. Chen, P. Jiang, X. Dong, J. Shi, Hierarchically porous bioactive glass scaffolds synthesized with a PUF and P123 cotemplated approach, Chem. Mater. 19 (17) (2007) 4322–4326, https://doi.org/10.1021/cm0708564.

[20] Y.F. Zhu, F.J. Shang, B. Li, Y. Dong, Y.F. Liu, M.R. Lohe, N. Hanagata, S. Kaskel, Magnetic mesoporous bioactive glass scaffolds: preparation, physicochemistry and biological properties, J. Mater. Chem. B 1 (9) (2013) 1279–1288, https://doi.org/10.1039/c2tb00262k.

[21] Y.F. Zhu, Y.F. Zhang, C.T. Wu, Y. Fang, J.H. Yang, S.L. Wang, The effect of zirconium incorporation on the physiochemical and biological properties of mesoporous bioactive glasses scaffolds, Microporous Mesoporous Mater. 143 (2–3) (2011) 311–319, https://doi.org/10.1016/j.micromeso.2011.03.007.

[22] C. Wu, W. Fan, Y. Zhu, M. Gelinsky, J. Chang, G. Cuniberti, V. Albrecht, T. Friis, Y. Xiao, Multifunctional magnetic mesoporous bioactive glass scaffolds with a hierarchical pore structure, Acta Biomater. 7 (10) (2011) 3563–3572, https://doi.org/10.1016/j.actbio.2011.06.028.

[23] J.R. Jones, S. Lin, S. Yue, P.D. Lee, J.V. Hanna, M.E. Smith, R.J. Newport, Bioactive glass scaffolds for bone regeneration and their hierarchical characterisation, Proc. Inst. Mech. Eng. H 224 (12) (2010) 1373–1387, https://doi.org/10.1243/09544119JEIM836.

[24] X. Chatzistavrou, O. Tsigkou, H.D. Amin, K.M. Paraskevopoulos, V. Salih, A.R. Boccaccini, Sol-gel based fabrication and characterization of new bioactive glass–ceramic composites for dental applications, J. Eur. Ceram. Soc. 32 (12) (2012) 3051–3061 https://doi.org/10.1016/j.jeurceramsoc.2012.04.037.

[25] X. Chatzistavrou, D. Esteve, E. Hatzistavrou, E. Kontonasaki, K.M. Paraskevopoulos, A.R. Boccaccini, Sol-gel based fabrication of novel glass-ceramics and composites for dental applications, Mater. Sci. Eng. C 30 (5) (2010) 730–739 https://doi.org/10.1016/j.msec.2010.03.005.

[26] T. Kokubo, H. Kushitani, S. Sakka, T. Kitsugi, T. Yamamuro, Solutions able to reproduce in vivo surface-structure changes in bioactive glass-ceramic A-W, J. Biomed. Mater. Res. 24 (6) (1990) 721–734, https://doi.org/10.1002/jbm.820240607.

[27] T. Kokubo, S. Ito, Z.T. Huang, T. Hayashi, S. Sakka, T. Kitsugi, T. Yamamuro, Ca, P-rich layer formed on high-strength bioactive glass-ceramic A-W, J. Biomed. Mater. Res. 24 (3) (1990) 331–343, https://doi.org/10.1002/jbm.820240306.

[28] V.C. Farmer, The Infrared Spectra of Minerals, Mineralogical Society of Great Britain and Ireland, London, 1974.

[29] V.K. Kaushik, Xps core level spectra and auger parameters for some silver compounds, J. Electron. Spectrosc. Relat. Phenom. 56 (3) (1991) 273–277, https://doi.org/10.1016/0368-2048(91)85008-H.

[30] A.L. Gonzalez, C. Noguez, Optical properties of silver nanoparticles, Phys. Status Solidi C - Curr. Top. Solid State Phys. 4 (11) (2007) 4118–4126, https://doi.org/10.1002/pssc.200675903.

[31] V. Karageorgiou, D. Kaplan, Porosity of 3D biomaterial scaffolds and osteogenesis, Biomaterials 26 (27) (2005) 5474–5491, https://doi.org/10.1016/j.biomaterials.2005.02.002.

[32] T.M. O'Shea, X.G. Miao, Preparation and characterisation of plga-coated porous bioactive glass-ceramic scaffolds for subchondral bone tissue engineering, Ceram. Mater. and Compon. Energy Environ. Appl (2010) 517, https://doi.org/10.1002/9780470640845.ch73 10.1002/9780470640845.ch73 210.

[33] J.R. Jones, E. Gentleman, J. Polak, Bioactive glass scaffolds for bone regeneration, Elements 3 (6) (2007) 393–399, https://doi.org/10.2113/Gselements.3.6.393.

[34] I. Tanahashi, M. Yoshida, Y. Manabe, T. Tohda, Effects of heat-treatment on Ag particle growth and optical-properties in Ag/Sio2 glass composite thin-films, J. Mater. Res. 10 (2) (1995) 362–365, https://doi.org/10.1557/Jmr.1995.0362.

[35] M.G. Garníca-Romo, J. González-Hernández, M.A. Hernández-Landaverde, Y.V. Vorobiev, F. Ruiz, J.R. Martínez, Structure of heat-treated sol-gel SiO2 glasses containing silver, J. Mater. Res. 16 (07) (2011) 2007–2012, https://doi.org/10.1557/jmr.2001.0275.

[36] T. Nakamura, K. Sameshima, K. Okunaga, Y. Sugiura, J. Sato, Determination of amorphous phase in quartz powder by X-ray powder diffractometry, Powder Diffr. 4 (1) (2013) 9–13, https://doi.org/10.1017/S0885715600016225.

[37] J. Serra, P. Gonzalez, S. Liste, S. Chiussi, B. Leon, M. Perez-Amor, H.O. Ylanen, M. Hupa, Influence of the non-bridging oxygen groups on the bioactivity of silicate glasses, J. Mater. Sci. Mater. Med. 13 (12) (2002) 1221–1225, https://doi.org/10.1023/A:1021174912802.

[38] J. Serra, P. Gonzalez, S. Liste, C. Serra, S. Chiussi, B. Leon, M. Perez-Amor, H.O. Ylanen, M. Hupa, FTIR and XPS studies of bioactive silica based glasses, J. Non-Cryst. Solids 332 (1–3) (2003) 20–27, https://doi.org/10.1016/j.jnoncrysol.2003.09.013.

[39] G. Laudisio, F. Branda, Sol–gel synthesis and crystallisation of 3CaO·2SiO2 glassy powders, Thermochim. Acta 370 (1–2) (2001) 119–124, https://doi.org/10.1016/s0040-6031(00)00786-3.

[40] O.M. Goudouri, M. Perissi, E. Theodosoglou, L. Papadopoulou, X. Chatzistavrou, E. Kontonasaki, P. Koidis, K.M. Paraskevopoulos, The impact of stirring rate on the crystallinity and bioactivity of 58S bioactive glass, Key Eng. Mater. 493–494 (2011) 43–48, https://doi.org/10.4028/.